Article

Spectroscopic–Electrical Combined Analysis to Assess the Conduction Mechanisms and the Performances of Metal Oxide Gas Sensors †

Ambra Fioravanti [1],*, Sara Morandi [2] and Maria Cristina Carotta [1]

1   Institute of Sciences and Technologies for Sustainable Energy and Mobility (CNR–STEMS), Via Canal Bianco 28, 44124 Ferrara, Italy
2   Department of Chemistry, University of Turin, Via P. Giuria 7, 10125 Torino, Italy
*   Correspondence: ambra.fioravanti@stems.cnr.it; Tel.: +39-0532-735668
†   This paper is an extended version of the conference paper: Fioravanti, A.; Morandi, S.; Carotta, M.C. Semiconductor Oxide Gas Sensors: Correlation between Conduction Mechanisms and Their Sensing Performances. In Proceedings of the 1st International Electronic Conference on Chemical Sensors and Analytical Chemistry (CSAC2021), 1–15 July 2021.

Abstract: Gas sensors that are based on metal oxides are extensively used to detect gaseous compounds in many different applications. One of the main tasks for improving the sensor performances is to understand the mechanism at the base of the sensing properties for each specific material. In this work, pure and mixed oxides were selected and synthesized in the form of nanometric powders. They were characterized by spectroscopic techniques, i.e., absorbance FT–IR and diffuse reflectance UV–Vis–NIR spectroscopies, to obtain information about the electronic properties and the type of defects that are involved at the root of the gas-sensing capabilities. The electrical characterization and the gas-sensing measurements were carried out on the related thick films. Finally, for each material, a description of the specific sensing mechanism is proposed by combining the characterization results.

1. Introduction

The adsorption of a gas on the surface of a semiconducting oxide can induce a significant change in the electrical resistance/conductance of the material [1]. This effect is at the basis of the development of the chemoresistors that are used for gas detection [2,3].

Due to their high sensitivity, tunable selectivity, easy production, small dimensions and low cost, they are successfully used in a broad range of applications such as pollutant monitoring [4,5], safety alert mechanisms [6], food quality control [7,8], industrial system control [9], and medical diagnosis [10,11] to detect the reducing and oxidizing gaseous compounds [12,13]. Despite this, an increasing demand for gas sensors with high performances has been documented [13] together with a higher research interest in them.

Many actions can be made to improve the sensing performances, primarily focusing the attention to the development of tailored functional materials. For example, it is possible to synthesize nanostructures with a smaller dimension [14], with a high specific surface area [15] by loading it with noble metals [16,17], but a very important issue is to determine the conduction and sensing mechanism of the materials at the base of their sensing properties [12,18].

In the electrical characterization, the main parameter that is typically measured is the conductance. All the operating characteristics of the sensors are derived from this measurement, considering the strength and the weakness of semiconductor sensors. On one hand, it is simple and easily measurable, while on the other hand, it is a second-order

parameter that, although it is very sensitive to some reactions at the solid surface, is not a direct indicator of the exact processes that are taking place.

For this reason, we investigated the behavior of different pure and mixed oxide materials by means of absorbance FT–IR and diffuse reflectance UV–Vis–NIR spectroscopies to enlighten the electronic properties.

The IR and UV–Vis spectroscopies represent effective experimental tools for investigating the electronic properties and surface chemistry of a broad group of metal oxides, being relevant for gas sensing [12,19,20]. When pure and perfectly stoichiometric, these oxides are insulating materials, transparent in the medium and near IR spectrum (MIR and NIR) and in the UV−Vis range up to the energy corresponding to the valence band (VB)—conduction band (CB) electronic transition. However, the presence of electronic levels that are close to the bottom of the CB (donors) or to the top of the VB (acceptors), arising from a variety of point defects, is responsible for their semiconducting properties and hence, for their gas sensing properties. The typical values for the activation energy of the donors and acceptors range from 10^{-3} to 10^{-1} eV. Therefore, it is possible to test these states by the absorption of the electromagnetic radiation at energies that are suitable to induce the electron photo-ionization from the donor levels to the CB or from the VB to the acceptor levels. Simultaneously, the presence of free carriers (electrons or holes) can be revealed by their characteristic continuous absorption of the radiation in the MIR range. Moreover, it is possible to detect the changes in the level populations and in the free carrier concentration by changing the temperature or the interacting atmosphere. The spectroscopic responses were studied in the range that spanned from room temperature (RT) to 500 °C both for the interaction with pure gas and for mixture target gas/O_2 at different concentrations depending on the specific oxide.

By coupling the spectroscopic results to those of the electrical characterization, we are able to describe the specific sensing mechanism for each studied material.

2. Materials and Methods

A selection of semiconducting oxides (single, such as SnO_2, WO_3 and TiO_2, or combined, such as Ti-Sn and W-Sn mixed oxides) were prepared through wet chemistry methods [21] using reagent-grade starting materials and solvents without any further purification.

WO_3 powder was prepared from a 0.02 M solution of WCl_6 (Merck) in absolute ethanol. After the addition of a small amount of 2,4-pentanedione (Merck), the solution was submitted to a warm treatment in a sonic bath and then to a rest of 2 h. The WO_3 precursor was filtered, washed with diethyl ether and dried at 90 °C for 12 h in air, then calcined at 650 °C for 2 h.

W-Sn mixed oxides were obtained by dissolving stoichiometric proportions of Tin(II) 2-ethylhexanoate (Merck, 97%) in a proper amount of 1-butanol and WCl_6 (Merck) in absolute ethanol. After the mixing of the two starting solutions, diluted HNO_3 was added to catalyze the hydrolysis process. The product was filtered, washed with diethyl ether and dried at 90 °C for 12 h in air, then it was calcined at 550 °C for 2 h.

In the following, we refer to samples with a Sn content of 10, 30, and 90% as WS10, WS30, and WS90, respectively.

SnO_2 synthesis starts by adding a given amount of deionized water drop by drop to a 1-butanol solution 0.7 M of tin(II)2-ethylexanoate (Merck, ~95%). The pH of the solution was maintained at 1 by the addition of HNO_3. After 3 h of stirring at room temperature, the solution was filtered and the resulting gel was dried at 90 °C for 12 h in air, then it was calcined at 550 °C for 2 h.

Ti-Sn mixed oxides were obtained by dissolving stoichiometric proportions of Sn(II)2-ethylexanoate (Merck, ~95%) ad Ti(IV) 1-butoxide (Merck, 97%) in a hydroalcoholic solution at a temperature of 50 °C under continuous stirring. Diluted acid was added to slightly modify the hydrolysis rate, and the resulting colloids were filtered, washed with diethyl ether and dried at 90 °C for 12 h in air. The resulting powders were calcined at 550 °C for 2 h.

In the following, we refer to samples with a Sn content of 10, 30, and 50 % as TS90, TS70, and TS50, respectively.

TiO$_2$ powder was prepared by dissolving Ti(IV) n-butoxide (Merck, 97%) in absolute ethanol (0.23 M). Subsequently, a solution ethanol/water in 1:1 vol. was added drop by drop under a rapid stirring condition to the first solution. The mixture was filtered, washed with diethyl ether and dried at 90 °C for 12 h in air, and then, it was calcined at 450 °C for 2 h.

The oxide powders were analyzed by using a Field Emission Scanning Electron Microscopy (FE-SEM) Carl Zeiss Sigma microscope operating at 3.00 kV for studying their morphology.

The crystalline structure and the average crystallite size were evaluated starting from the X-ray diffraction (XRD) patterns that were collected using a PW 3830/3020 X'Pert Diffractometer (PANalytical) working with Bragg-Brentano geometry and using the Cu Kα_1 radiation (λ = 1.5406 Å). In particular, the values of average crystallite size were calculated by Williamson–Hall method which was applied to the XRD patterns [22].

The specific surface areas (SSA) were determined by applying the Brunauer–Emmett–Teller (BET) method to the adsorption/desorption isotherms of N$_2$ at 77 K which were obtained using a Micromeritics ASAP 2010 physisorption analyzer.

The powders were characterized by means of spectroscopic techniques with the aim to evaluate the electronic properties and defects that are involved in the sensing processes.

Absorbance IR spectra were collected using a Perkin–Elmer System 2000 FT–IR spectrophotometer, which was equipped with a Hg–Cd–Te cryodetector, and that was working in the range of wavenumbers 7800–580 cm^{-1}. For IR analysis, the powders were compressed in self-supporting discs ($\sim$20 mg/cm^2) and placed in a commercial stainless steel IR cell (Aabspec).

Diffuse reflectance spectra in the UV–Vis–NIR region were run using a Varian Cary 5 spectrophotometer that was working in the range of wavenumbers 53000–4000 cm^{-1}. Spectra are reported as Kubelka–Munk function [f(R$_\infty$) = (1 − R$_\infty$)2/2R$_\infty$, where R$_\infty$ is the reflectance of an "infinitely thick" layer of the sample] in the ordinate scale.

The spectroscopic responses were studied in the range that spanned from room temperature to 500 °C both for the interaction with pure gases and for mixture gas/O$_2$ at different concentrations depending on the oxide [23,24].

For obtaining thick films for electrical characterization and gas sensing measurements, the functional materials were added to an organic vehicle together with a small percentage of glass frit. Then, they were deposited on alumina substrates with interdigitated Au contacts and a heating element, and they were finally fired at 650 °C. The flow-through technique was used by maintaining a flow rate of 0.5 L/min, using synthetic air as carrier gas in dry conditions for the: (i) conductance measurements vs. temperature (Arrhenius plot) in the range room temperature −650 °C; (ii) surface potential barrier height measurements to determine the intergranular energy barrier (Schottky barrier) versus temperature, following the method of stimulated temperature conductance measurements that was described by Clifford and Tuma [23,25]; (iii) dynamical responses which were obtained in the presence of a mixture of different gases and operating temperature from 350 to 550 °C. The sensor response was calculated as the ratio between the conductance in the presence of the gas test and the conductance in air.

In this work, we selected the carbon monoxide (CO) as gas test for all the materials and for all the characterizations.

Finally, a sensing mechanism was proposed for each material by combining the results of spectroscopic characterization and those of electrical characterization.

3. Results and Discussion

3.1. Material Characterizations

The SEM observations showed a homogeneous distribution in the size and shape and a good agreement with the crystallite sizes and SSA for all the oxide powders [23,24,26].

They are constituted by spherical particles with a grain size that ranges from 20 to 40 nm for SnO_2 and TiO_2 and from 60 to 90 nm for WO_3.

In the case of the (Ti-Sn) mixed oxides, the SEM analysis shows grains with very small diameters (from 10 to 30 nm). Among the W-Sn mixed oxides, the largest particles are those of the WS10 sample (average diameter 40 nm), while for the two samples with higher amount of Sn content, the mean diameter decreased down to 20 nm.

The crystalline structures of the samples are reported in Table 1 along with the mean crystallite sizes, which were calculated by Williamson–Hall method applied to the XRD patterns and the specific surface areas (SSA). All the samples are characterized by a single crystalline phase. As for W-Sn mixed oxides, the highest surface area, i.e., the smallest crystallite size is shown by WS90, which is the only one W-Sn mixed sample with the same crystalline structure of SnO_2. As for Ti-Sn mixed oxides, the SSA increased with the increasing of Ti content with the rutile tetragonal phase maintained in all the TS samples.

Table 1. Crystalline phases, space groups, mean crystallite sizes, and specific surface areas of the pure and mixed oxides.

Sample	Cryst. Phase	Space Group	Cryst. Size (nm)	SSA (m^2/g)
WO_3	Monoclinic pseudo-cubic	P 1 2_1/n 1	85.0	9.7
WS10	Monoclinic pseudo-cubic	P 1 2_1/n 1	24.0	24.5
WS30	Monoclinic pseudo-cubic	P 1 2_1/n 1	27.0	16.4
WS90	Tetragonal	P 4_2/mnm	6.0	72.0
SnO_2	Tetragonal	P 4_2/mnm	12.0	27.9
TS90	Tetragonal (Rutile)	P 4_2/mnm	7.8	45.4
TS70	Tetragonal (Rutile)	P 4_2/mnm	4.4	87.8
TS50	Tetragonal (Rutile)	P 4_2/mnm	4.4	99.0
TiO_2	Tetragonal (Anatase)	I 4_1/amd	8.0	121.2

3.2. Combined Electical with Spectroscopic Characterizations for Pure Oxides

SnO_2, WO_3, and TiO_2, which are taken into consideration in this work, are n-type semiconductor oxides that are characterized by the presence of free electrons in the conduction band, mainly due to lattice defects that are generated by reducing the processes during the synthesis of the materials. Such basic properties are analyzed, taking into account the mechanism of the conduction that is generally accepted for the metal oxide semiconductors in the form of nanoparticles: the presence of the charged surface states, mainly due to the energy levels that were introduced by oxygen within the band gap, is the origin of the surface potential barriers (Schottky barriers), which are crossed only by those electrons that had a sufficient energy. Such electron flows take part in the electrical conductance at the surface through a huge series of intergranular point contacts. The chemoresistivity is at the base of the sensing mechanism, which consists of a variation of the intergranular barrier with a subsequent conductance modification occurring as a response to surface chemical reactions with the environmental gases [27].

The Arrhenius plots that are reported in Figure 1a confirm for all of the materials the n-type semiconductor behavior; SnO_2 and WO_3 exhibiting three regions of conductance with the SnO_2 conductance value, at low temperature, almost three orders of magnitude lower than the WO_3 one. TiO_2 exhibits an Arrhenius plot that is very different from the others especially since the behavior toward the temperature does not appear to be influenced by the surface potential barrier formation, and therefore, by the ionosorption of the oxygen atoms. Moreover, the conductance values at 600 K, exhibit four orders-of-magnitude lower than those for SnO_2.
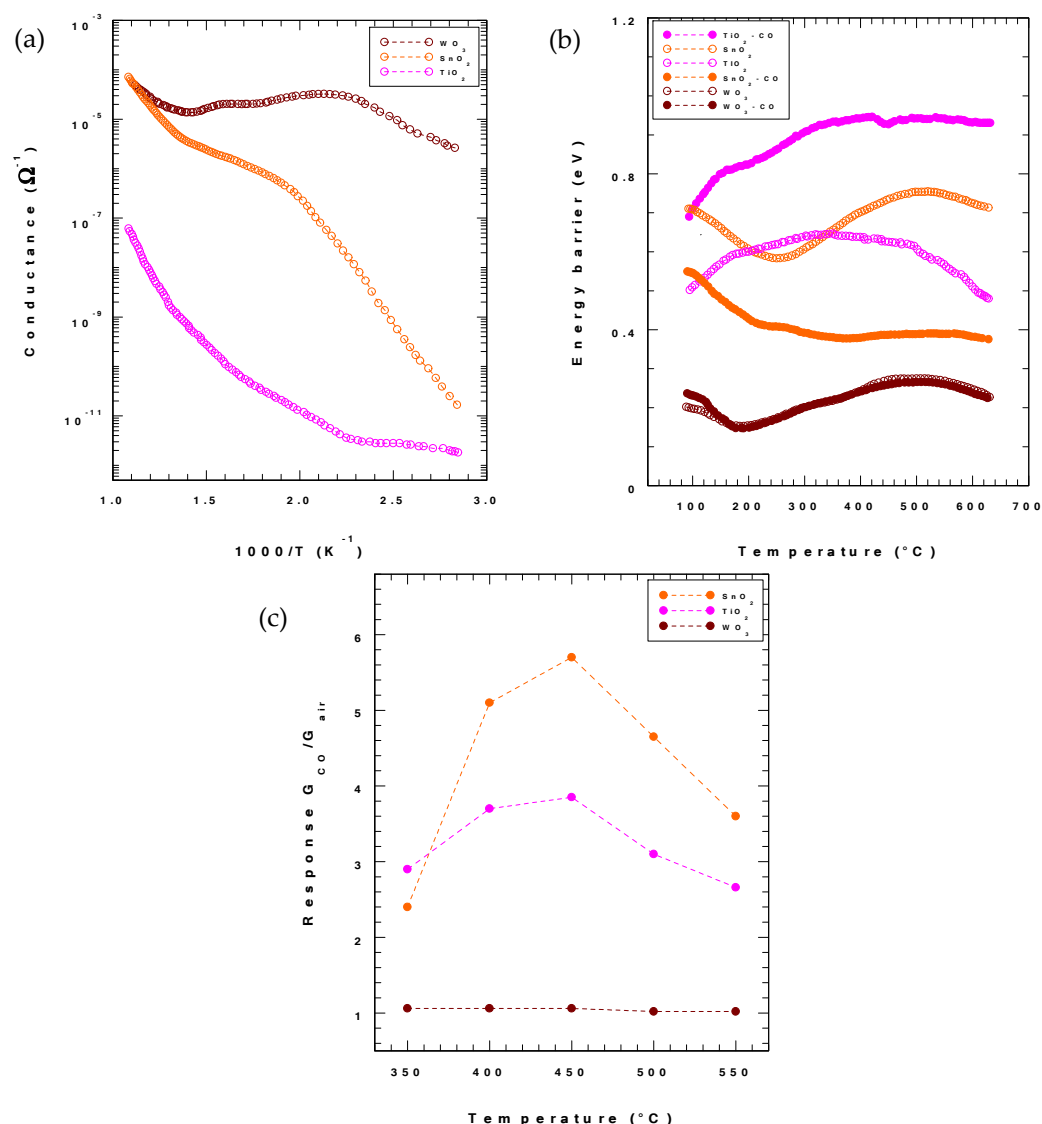
Figure 1. Conductance vs. temperature in dry air (**a**), comparison between the energy barrier dependence on temperature in dry air and in a mixture of dry air and CO (100 ppm) (**b**), responses to 50 ppm of CO reported as G_{CO}/G_{air} obtained at different temperatures (**c**) for the pure oxides.

By observing the corresponding curves of the energy barrier as a function of temperature, and by comparing those in dry air with those in the mixture of dry air and carbon monoxide, some observations can be made: (i) SnO_2 and WO_3 exhibit a similar trend vs. temperature, but with lower values in the case of WO_3; (ii) comparing the energy barrier values in dry air or in the mixture of dry air and CO, such values are very different in SnO_2 for which the barrier decreases after the surface chemical reaction with carbon monoxide (due to the transfer of electrons in the conduction band), while in WO_3 such mechanism is almost absent; (iii) the case of TiO_2 appears different for two reasons. On one hand, the shape of the energy barrier vs. temperature does not exhibit the usual trend that is characterized by a minimum and a maximum value within the temperatures of 200–450 °C (corresponding to the transformation from O_2^- to O^- adsorption on the semiconductor surface). On the other hand, contrary to the usual for a n-type semiconductor, the chemical reaction with carbon monoxide provides an increase of the barrier values rather than a decrease of them.

The spectroscopic characterization on the single oxides, which is carried out in the UV–Vis–NIR and medium IR regions, highlights the presence of defect levels in the band

gap of the materials. In the case of SnO_2, the broad absorption centered at about 1650 cm^{-1} has been assigned to the photo-ionization of the mono-ionized oxygen vacancies [28], thus revealing the presence of electronic levels at about 0.2 eV below the conduction band. Similarly, in WO_3, the electronic levels that are related to the absorption observed at about 4500 cm^{-1} have been associated with the polarons that are localized in the band gap at 0.55 eV below the conduction band [24]. Such difference should cause a lower energy barrier in WO_3 with respect to SnO_2, being the barrier height determined by the difference between the Fermi level of the surface states and the Fermi level in the bulk. Effectively, this behavior has been verified (see Figure 1b) so justifying the higher conductivity that is observed in the Arrhenius plots of Figure 1a. Figure 1c reports the response values of the dynamical measurements carried out in presence of 50 ppm of carbon monoxide in dry air. The WO_3-based sensors highlight an insignificant response to CO, confirming the result obtained comparing the energy barrier measurement in air and in the mixture of air and CO. When the barrier height does not change after the contact with chemisorbed surface species from the environment, the "pinning of the Fermi level" phenomenon is observed, thus causing an insignificant change in the conductivity of the semiconductor [29]. Generally, the functional materials that are characterized by a very low energy barrier, as in the case of WO_3, are more suitable for detecting the oxidizing gases, resulting favored the release of electrons from the conduction band. As mentioned above, Figure 1b shows a very strange behavior of the TiO_2 energy barrier, which consists of an increasing in the barrier when a reducing gas as carbon monoxide was in contact with the semiconductor surface instead of a decrease due to the electron transfer in the conduction band and the increase in the conductivity. Additionally, this phenomenon can be interpreted by means of the spectroscopic analysis.

Looking at the spectroscopic responses of TiO_2 to CO, which is reported in Figure 2, it is evident a very broad absorption extending from the visible to medium IR region. This means that for the TiO_2 electronic levels at different deepness in the band gap, such as Ti^{3+} polarons and oxygen vacancies, can be identified [30].
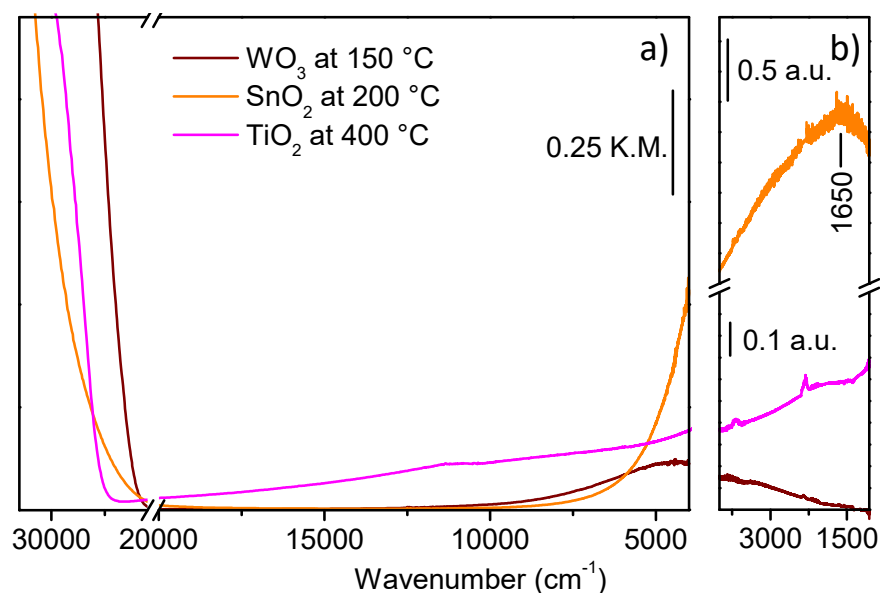
Figure 2. UV–Vis–NIR (**a**) and medium IR (**b**) spectra of: (i) WO_3 and SnO_2 during interaction with CO/O_2 (1:5, pCO = 5 mbar) mixture at the temperature of the maximum intensity reached by the main electronic absorption; (ii) TiO_2 during interaction with CO (20 mbar) at 400 °C.

It has to be noted that the spectra for SnO_2 and WO_3 (see Figure 2) show the maximum intensity of the main electronic absorption during the interaction with the mixture of CO/O_2 at a relatively low temperature (150–200 °C). To reach the same intensity of absorption in TiO_2, it has been necessary to operate in a strongly reducing atmosphere (pure CO) and at a

higher temperature (400 °C). Therefore, only in these extreme conditions we can obtain the absorptions that are related to oxygen vacancies and Ti^{3+} polarons and not in the typical working conditions. This behavior must be related to a different sensing mechanism, which could be the same of the Ti-Sn mixed oxides, which is discussed in the next section.

3.3. Combined Electical with Spectroscopic Characterizations for Mixed Oxides

Now we consider the functional materials and the relative thick film sensors that were obtained by synthesizing the mixed oxides (W-Sn) and (Ti-Sn) as described in Section 2. In Figure 3a, the Arrhenius plots for WS10, WS30, and WS90 thick films obtained in dry air atmosphere, are reported.
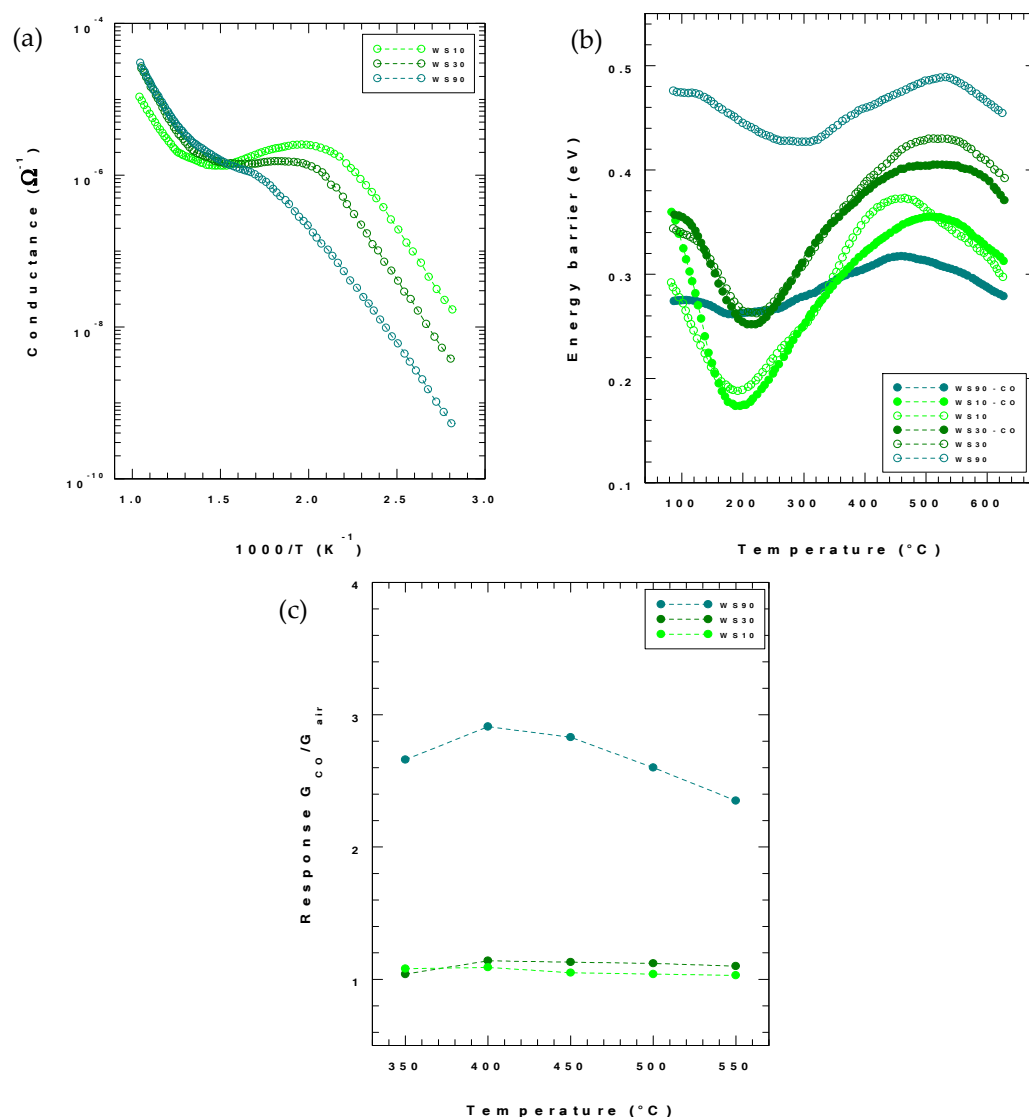
Figure 3. Conductance vs. temperature in dry air (**a**), comparison between the energy barrier dependence on temperature in dry air and in a mixture of dry air and CO (100 ppm) (**b**), responses to 50 ppm of CO reported as G_{CO}/G_{air} obtained at different temperatures (**c**) for W-Sn mixed oxides.

All of the mixed oxides exhibited an intermediate conductivity between the SnO_2 and WO_3 ones. In particular, WS10 behaved similarly to WO_3, WS90 behaved similarly to SnO_2, while the Arrhenius of the WS30 film remained in-between. To justify this result, we have to consider the spectroscopic results through which the defect level deepness in the band gap of WS10, WS30, and WS90 has been measured. Figure 4 shows the UV–Vis–NIR and IR spectra of the W-Sn mixed oxides in their interaction with CO/O_2. All samples are

characterized by the formation of a broad band that is related to the electronic transition from defect levels in the band gap to the C.B. The position of the bands allows us to calculate the deepness of the levels in the band gap. Precisely, the defect levels of WS10 and WS30 are located at the same value of pure WO_3 at 0.55 eV below the conduction band, while those of WS90 at 0.28 eV, value closer to the SnO_2 one.
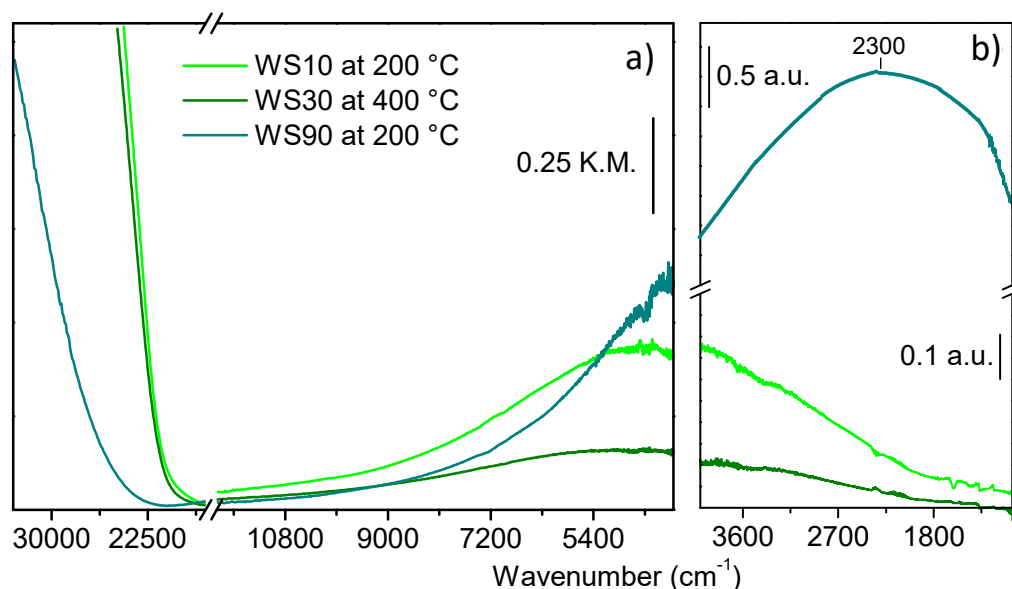
Figure 4. UV–Vis–NIR (**a**) and medium IR (**b**) spectra of WS10, WS30, and WS90 during interaction with CO/O_2 (1:5, p_{CO} = 5 mbar) mixture at the temperature of the maximum intensity reached by the main electronic absorption.

WS10 and WS90 are perfectly in line with expectations, while WS30 slightly differs; it is thereby convenient to compare the related energy barriers, shown in Figure 3b, which trend turns out more in agreement with the spectroscopic results. On the other hand, the WS90 energy barrier height seems too much different from that of SnO_2 considering their respective energy levels. However, in this case, another phenomenon could be taken into consideration. Indeed, the grain size of WS90 could be comparable with the depletion layer width, thus not allowing the complete band bending development and therefore, resulting a lower Schottky barrier [31]. By comparing the energy barriers in air or in the mixture of air and CO, no significant effect is observable both in WS10 and WS30, which behave like pristine WO_3. Different is obviously the case of WS90, showing some sensitivity to CO due to its structure closer to SnO_2 than to WO_3. This fact is confirmed by the responses of the dynamical measurements that are reported in Figure 3c.

By examining the mixed oxides Ti-Sn, the Arrhenius plots of Figure 5a show that in dry air, the conductance decreased by increasing the titanium content in the mixed oxide up to four orders-of-magnitude. Moreover, the shape of the Arrhenius plot changed as a minimum content of titanium was added to tin dioxide (TS90). However, TS90 preserved a trend similar to SnO_2 with different conductivity regions demonstrating the occurrence of different surface adsorption phenomena, while TS70 and TS50 show a similar behavior to that of pure TiO_2. However, it must be noted that pure TiO_2 that was heated at 650 °C remained in an anatase crystalline phase, whilst all the mixed oxides calcined at 550 °C exhibited a rutile phase.
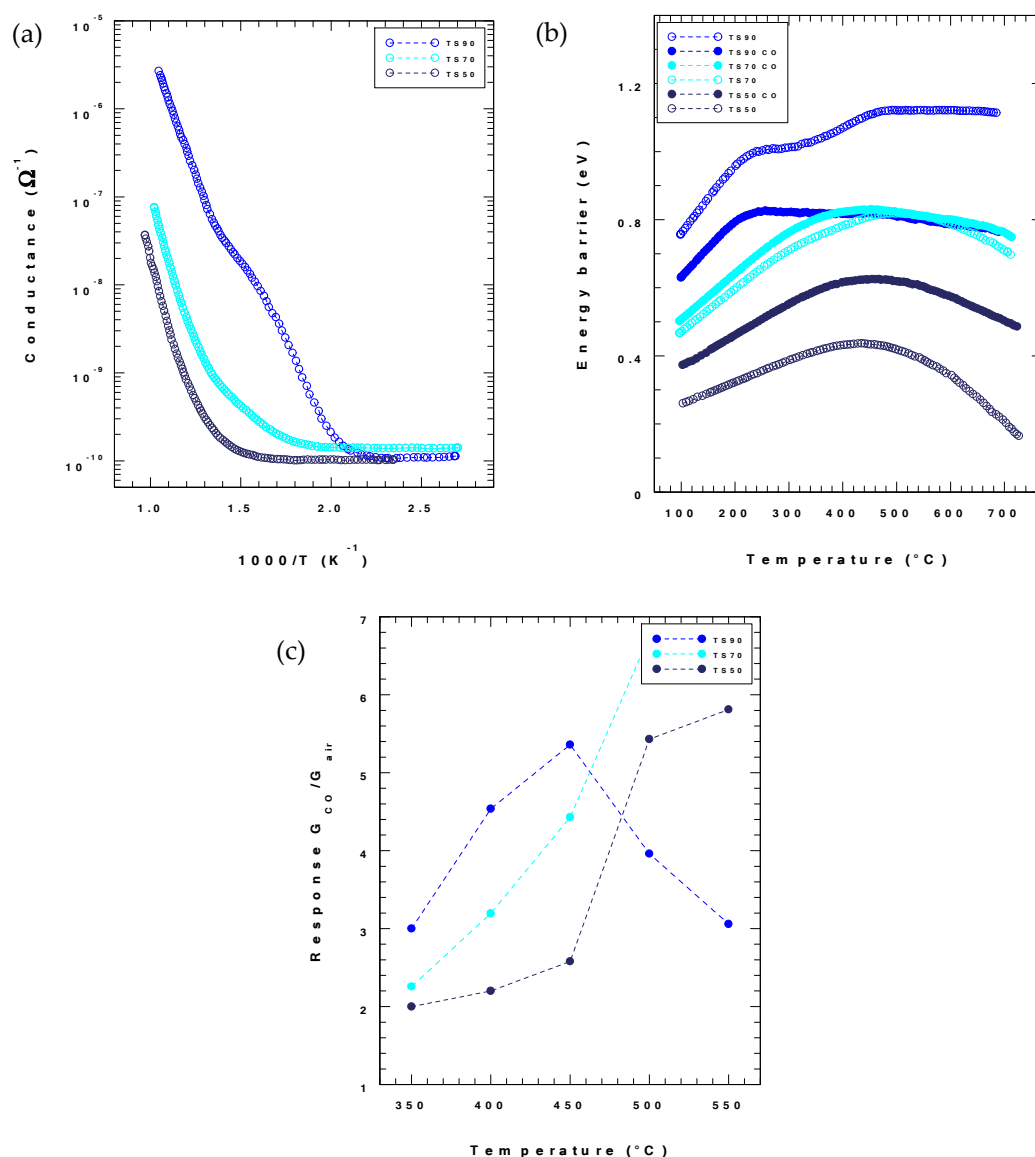
Figure 5. Conductance vs. temperature in dry air (**a**), comparison between the energy barrier dependence on temperature in dry air and in a mixture of dry air and CO (100 ppm) (**b**), responses to 50 ppm of CO reported as G_{CO}/G_{air} obtained at different temperatures (**c**) for the Ti-Sn mixed oxides.

Figure 5b shows the heights of the potential barriers as function of temperature both in air and in the mixture of air and CO. As in the case of the Arrhenius plots, TS90 still behaves like SnO_2, in particular with respect to the decreasing of the barrier after the contact with carbon monoxide due to the transfer of electrons from the surface to the conduction band as a consequence of the surface chemical reaction with the gas. On the contrary, both TS70 and TS50 exhibit the same feature that was already described for pure TiO_2: the barrier height in CO turns out to be above the barrier in the air, thereby making the Schottky barrier mechanism not exactly working for the pure TiO_2. Additionally, the mixed oxides with a content of Ti atoms starting from about 30% behave similarly.

The explanation for this phenomenon has been found in the spectroscopic responses in the medium IR region (see Figure 6).
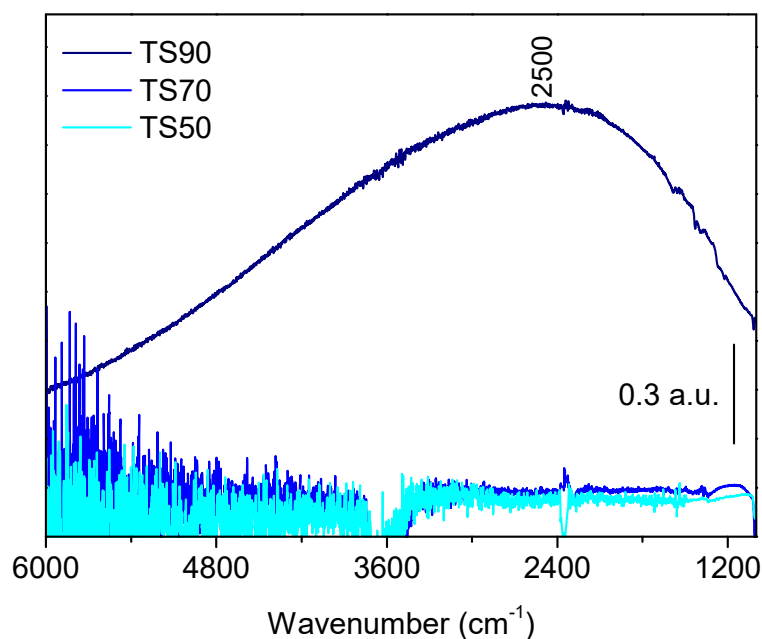
Figure 6. IR spectra recorded during CO (20 mbar) interaction at 200 °C for TS90 and at 400 °C for TS70 and TS50.

Indeed, TS90 after the CO interaction, just as SnO_2, shows an increase of a broad absorption with maximum at about 2500 cm^{-1}, assigned to the photo-ionization of mono-ionized oxygen vacancies, as discussed above. On the contrary, both the TS70 and TS50 samples do not show any electronic absorption, but an erosion of the absorption edge that is related to the skeletal vibrational modes as reported in our previous paper [28]. This erosion is ascribable to the loss of reticular oxygen near the surface during the reducing treatment in CO. Due to this phenomenon, the assessment of carbon monoxide sensitivity through the comparison between the barriers in air or in the mixture of air and testing gas could be incorrect. However, the dynamical measurements performed in 50 ppm of carbon monoxide in dry air reported enhanced responses for TS70 with respect to TS50 even if the SSA of TS50 is higher than that of TS70 (see Table 1). Therefore, in this specific mixed oxide, the grain size did not result the main parameter for obtaining optimized gas sensitivity. Indeed, the Ti content in the functional material is a second important parameter to be considered in the sensing process.

The spectroscopic measurements highlighted two competing mechanisms: the reaction of CO with ionosorbed oxygen atoms (and hence, the Schottky barrier electron conduction) and the reaction of CO with the surface lattice oxygen atoms which bound electrons enter in the conduction band without affecting the barrier height, but only, the bulk conductance. To conclude, it turned out that the Ti-Sn new compounds provide improved gas responses compared to those of pure TiO_2 and also to those of pure SnO_2. Moreover, the sensing properties resulted tunable through the titanium content that is in the mixed oxide.

4. Conclusions

We successfully prepared three single oxides (SnO_2, WO_3, and TiO_2), three mixed oxides W-Sn with different Sn content, and three mixed oxides Ti-Sn with different Sn content, obtaining a single crystalline phase for each material. The behaviors of these materials were investigated by means of IR and UV−Vis spectroscopies in a reducing atmosphere to enlighten the electronic properties and the defects that are involved in the gas sensing. By coupling these results with those obtained from the electrical characterization, we can describe the sensing behavior of these oxides.

The spectroscopic characterization highlighted the presence of defect levels deeper in the band gap for WO_3 with respect to those of SnO_2. This is in agreement with the higher

conductance, the lower energy barrier and the reduced sensitivity to CO in WO_3. Among the W-Sn mixed oxides, WS10 behaved like WO_3, WS90 behaved like SnO_2, and WS30 is in-between. For these oxides, the Schottky barrier conduction mechanism well describes their behavior.

In the case of the TiO_2 and Ti-Sn mixed oxides, their conductance decreases with the Ti content. TS90 showed a behavior similar to that of SnO_2, while the TS70 and TS50 ones similar to that of TiO_2. In this case, for which the barrier height in CO is above that in air, the Schottky barrier conduction mechanism cannot completely describe this behavior. A second mechanism must be taken into account for which the CO reacts with the surface lattice oxygen atoms. The bound electrons of these atoms enter in the conduction band without affecting the barrier height, but only, the bulk conductance.

Finally, the possibility to describe the processes that are involved in the detection mechanism of the sensors with a method of combined characterizations was shown. This method can be applied to every functional material and every gas of interest.

Author Contributions: Conceptualization, characterizations, experiments conduction and data analysis A.F., S.M. and M.C.C.; writing—original draft preparation A.F. All authors have read and agreed to the published version of the manuscript.

Institutional Review Board Statement: Not applicable.

Informed Consent Statement: Not applicable.

Data Availability Statement: Not applicable.

Conflicts of Interest: The authors declare no conflict of interest.

References

1. Seiyama, T.; Fujiishi, K.; Nagatani, M.; Kato, A. A New Detector for Gaseous Components Using Zinc Oxide Thin Films. *J. Soc. Chem. Ind. Japan* **1963**, *66*, 652–655. [CrossRef]
2. Taguchi, N. UK Patent 1280809, 1970.
3. Neri, G. First fifty years of chemoresistive gas sensors. *Chemosensors* **2015**, *3*, 1–20. [CrossRef]
4. Fioravanti, A.; Bonanno, A.; Gherardi, S.; Carotta, M.C.; Skouloudis, A.N. A portable air-quality station based on thick film gas sensors for real time detection of traces of atmospheric pollutants. In Proceedings of the IOP Conference Series: Materials Science and Engineering, Mykonos, Greece, 27–30 September 2016; Volume 108.
5. Djedidi, O.; Djeziri, M.A.; Morati, N.; Seguin, J.L.; Bendahan, M.; Contaret, T. Accurate detection and discrimination of pollutant gases using a temperature modulated MOX sensor combined with feature extraction and support vector classification. *Sens. Actuators B Chem.* **2021**, *339*, 129817. [CrossRef]
6. Firtat, B.; Moldovan, C.; Brasoveanu, C.; Muscalu, G.; Gartner, M.; Zaharescu, M.; Chesler, P.; Hornoiu, C.; Mihaiu, S.; Vladut, C.; et al. Miniaturised MOX based sensors for pollutant and explosive gases detection. *Sens. Actuators B Chem.* **2017**, *249*, 647–655. [CrossRef]
7. Galstyan, V.; Ponzoni, A.; Kholmanov, I.; Natile, M.M.; Comini, E.; Sberveglieri, G. Highly sensitive and selective detection of dimethylamine through Nb-doping of TiO2 nanotubes for potential use in seafood quality control. *Sens. Actuators B Chem.* **2020**, *303*, 127217. [CrossRef]
8. Love, C.; Nazemi, H.; El-Masri, E.; Ambrose, K.; Freund, M.S.; Emadi, A. A Review on Advanced Sensing Materials for Agricultural Gas Sensors. *Sensors* **2021**, *21*, 3423. [CrossRef] [PubMed]
9. Fioravanti, A.; Marani, P.; Massarotti, G.P.; Lettieri, S.; Morandi, S.; Carotta, M.C. (Ti,Sn) solid solution-based gas sensors for new monitoring of hydraulic oil degradation. *Materials* **2021**, *14*, 605. [CrossRef]
10. Dong, H.; Qian, L.; Cui, Y.; Zheng, X.; Cheng, C.; Cao, Q.; Xu, F.; Wang, J.; Chen, X.; Wang, D. Online Accurate Detection of Breath Acetone Using Metal Oxide Semiconductor Gas Sensor and Diffusive Gas Separation. *Front. Bioeng. Biotechnol.* **2022**, *10*, 861950. [CrossRef]
11. Lawson, B.; Aguir, K.; Fiorido, T.; Martini-Laithier, V.; Bouchakour, R.; Burtey, S.; Reynard-Carette, C.; Bendahan, M. Skin alcohol perspiration measurements using MOX sensors. *Sens. Actuators B Chem.* **2019**, *280*, 306–312. [CrossRef]
12. Dey, A. Semiconductor metal oxide gas sensors: A review. *Mater. Sci. Eng. B Solid-State Mater. Adv. Technol.* **2018**, *229*, 206–217. [CrossRef]
13. Fioravanti, A.; Carotta, M.C. Year 2020: A snapshot of the last progress in flexible printed gas sensors. *Appl. Sci.* **2020**, *10*, 1741. [CrossRef]

14. Yamazoe, N.; Shimanoe, K. *Fundamentals of Semiconductor Gas Sensors*, 2nd ed.; Elsevier: Amsterdam, The Netherlands, 2019; ISBN 9780081025598.

15. Fioravanti, A.; Bonanno, A.; Mazzocchi, M.; Carotta, M.C.; Sacerdoti, M. Enhanced Gas Sensing Properties of Different ZnO 3D Hierarchical Structures. *Adv. Sci. Technol.* **2016**, *99*, 48–53. [CrossRef]

16. Degler, D.; Weimar, U.; Barsan, N. Current Understanding of the Fundamental Mechanisms of Doped and Loaded Semiconducting Metal-Oxide-Based Gas Sensing Materials. *ACS Sens.* **2019**, *4*, 2228–2249. [CrossRef] [PubMed]

17. Wu, K.; Debliquy, M.; Zhang, C. Room temperature gas sensors based on Ce doped TiO2 nanocrystals for highly sensitive NH3 detection. *Chem. Eng. J.* **2022**, *444*, 136449. [CrossRef]

18. Galstyan, V. "Quantum dots: Perspectives in next-generation chemical gas sensors"—A Review. *Anal. Chim. Acta* **2021**, *1152*, 238192. [CrossRef]

19. Barhoum, A. *Optical Spectroscopy for Characterization of Metal Oxide Nanofibers*; Springer: Berlin/Heidelberg, Germany, 2019; ISBN 9783319536545.

20. Yang, C.; Wöll, C. IR spectroscopy applied to metal oxide surfaces: Adsorbate vibrations and beyond. *Adv. Phys. X* **2017**, *2*, 373–408. [CrossRef]

21. Nikam, A.V.; Prasad, B.L.V.; Kulkarni, A.A. Wet chemical synthesis of metal oxide nanoparticles: A review. *CrystEngComm* **2018**, *20*, 5091–5107. [CrossRef]

22. Suryanarayana, C.; Norton, M.G. *X-Ray Diffraction: A Practical Approach*; Springer: New York, NY, USA, 1998; ISBN 9781489901507.

23. Carotta, M.C.; Fioravanti, A.; Gherardi, S.; Malagù, C.; Sacerdoti, M.; Ghiotti, G.; Morandi, S. (Ti,Sn) solid solutions as functional materials for gas sensing. *Sens. Actuators B Chem.* **2014**, *194*, 195–205. [CrossRef]

24. Morandi, S.; Amodio, A.; Fioravanti, A.; Giacomino, A.; Mazzocchi, M.; Sacerdoti, M.; Carotta, M.C.; Skouloudis, A.N. Operational functionalities of air-quality W–Sn metal-oxide sensors correlating semiconductor defect levels and surface potential barriers. *Sci. Total Environ.* **2020**, *706*, 135731. [CrossRef]

25. Clifford, P.K.; Tuma, D.T. Characteristics of semiconductor gas sensors II. transient response to temperature change. *Sens. Actuators* **1982**, *3*, 255–281. [CrossRef]

26. Fioravanti, A.; Morandi, S.; Pedrazzo, A.R.; Cecone, C.; Manzoli, M.; Zanetti, M.; Bracco, P.; Mazzocchi, M.; Lettieri, S.; Marani, P.; et al. Investigation of the key parameters for gas sensing through comparison of electrospun and sol-gel semiconducting oxides. *Ceram. Int.* **2022**, *48*, 20948–20960. [CrossRef]

27. Madou, M.J.; Morrison, S.R. *Chemical Sensing with Solid State Devices*; Academic Press Inc.: Cambridge, MA, USA, 1989; ISBN 0124649653.

28. Carotta, M.C.; Cervi, A.; Gherardi, S.; Guidi, V.; Malagu', C.; Martinelli, G.; Vendemiati, B.; Sacerdoti, M.; Ghiotti, G.; Morandi, S.; et al. (Ti, Sn) O^2 solid solutions for gas sensing: A systematic approach by different techniques for different calcination temperature and molar composition. *Sens. Actuators B Chem.* **2009**, *139*, 329–339. [CrossRef]

29. Malagù, C.; Carotta, M.C.; Comini, E.; Faglia, G.; Giberti, A.; Guidi, V.; Maffeis, T.G.G.; Martinelli, G.; Sberveglieri, G.; Wilks, S.P. Photo-induced unpinning of fermi level in WO$_3$. *Sensors* **2005**, *5*, 594–603. [CrossRef]

30. Pacchioni, G. Oxygen Vacancy: The Invisible Agent on Oxide Surfaces. *ChemPhysChem* **2003**, *4*, 1041–1047. [CrossRef] [PubMed]

31. Malagù, C.; Carotta, M.C.; Galliera, S.; Guidi, V.; Maffeis, T.G.G.; Martinelli, G.; Owen, G.T.; Wilks, S.P. Evidence of bandbending flattening in 10 nm polycrystalline SnO$_2$. *Sens. Actuators B Chem.* **2004**, *103*, 50–54. [CrossRef]